

Probing the Spatial Impulse Response of Ultrahigh-Frequency Ultrasonic Transducers with Photoacoustic Waves


Qiang-Bing Lu¹, Tuo Liu^{2,3}, Lei Ding¹, Ming-Hui Lu^{1,4,*}, Jie Zhu^{2,3,†} and Yan-Feng Chen¹

¹*Department of Materials Science and Engineering, and National Laboratory of Solid State Microstructures, Nanjing University, Nanjing 210093, China*

²*Research Center for Fluid-Structure Interactions, Department of Mechanical Engineering, The Hong Kong Polytechnic University, Hung Hom, Kowloon, Hong Kong SAR, China*

³*The Hong Kong Polytechnic University Shenzhen Research Institute, Shenzhen 518057, China*

⁴*Jiangsu Key Laboratory of Artificial Functional Materials, Nanjing University, Nanjing 210093, China*

 (Received 17 May 2020; revised 22 July 2020; accepted 7 August 2020; published 10 September 2020)

Characterizing the radiated or received acoustic field of ultrasonic transducers using the spatial impulse response (SIR) represents an important step in testing, design, and optimization of ultrasonic transducers. However, for the ultrahigh-frequency acoustic field, conventional methods, such as the hydrophone method and the small-ball reflection method, are limited by narrow bandwidth and poor spatial resolution. Here, we propose a method to obtain the transducer's SIR through its response to photoacoustic waves, which allows high-precision acoustic field measurements, with spatial resolution as fine as $1.7 \mu\text{m}$. We subsequently measure the SIRs of two focused ultrasonic transducers, with 20 and 93 MHz center frequencies, and confirm that the three-dimensional acoustic fields can be accurately reconstructed using the angular spectrum approach. More importantly, this method is unique to receive-only ultrasonic detectors, the SIR of which could not be measured previously with conventional methods, and it could facilitate ultrasonic transducer design, as well as other related fields, such as nondestructive evaluation, biomedical imaging, and particle manipulation.

DOI: [10.1103/PhysRevApplied.14.034026](https://doi.org/10.1103/PhysRevApplied.14.034026)

I. INTRODUCTION

As a kind of component for mutual conversion between mechanical energy and electrical power, ultrasonic transducers have wide applications in photoacoustic imaging [1], nondestructive testing [2], ultrasound imaging [3], fluid-flow measurements [4], and so on [5]. Different application scenarios have specific requirements for the radiated or received acoustic field (or directivity) of a transducer. Characterizing it as precisely as possible is thus of great importance for designing and manufacturing more advanced transducers [6,7], and it is also helpful to improve imaging quality by means of beam forming [8] and synthetic aperture [9]. Nowadays, acoustic field simulation and calculation tools, for instance, Field II [10] and k-Wave [11] are widely used in engineering and science. Nevertheless, the actual acoustic field must be obtained through experimental measurement.

Currently, there are two main methods, the hydrophone (HP) method [12] and the small-ball reflection (BR) method [13], used for measuring the radiated acoustic fields of transducers. For the HP method, the relatively large detection area, averaging the amplitude of the acoustic field, causes poor spatial resolution at the hundreds or tens of microns scale [14]. Meanwhile, due to the limited frequency response of a hydrophone [15], it is difficult to accurately record the high-frequency component of the transducer's impulse response. For the BR method, the spatial resolution determined by the effective reflection area of a stainless-steel ball declines as the small ball approaches the transducer surface [16]. On the other hand, a smaller ball will lead to a decreased signal-to-noise ratio (SNR), despite its ability to improve the spatial resolution. Additionally, both methods require the transducer to operate in a transmit mode. They are incapable of characterizing receive-only ultrasonic detectors.

According to the acoustic reciprocity theorem [17–19], the radiated and received acoustic fields of a transducer are reciprocal and can be comprehensively characterized by its spatial impulse response (SIR), which contains both

*luminghui@nju.edu.cn

†jiezhu@polyu.edu.hk

spatial and spectral information [20,21]. The SIR of a transducer can be obtained by using an ideal-point ultrasonic detector to record the pulsed pressure waves generated by the transducer itself excited by a delta function, $\delta(t)$, in a transmit mode or using the transducer itself to record the pulsed spherical pressure wave emitted from a point acoustic source in a received mode. In the latter scenario, the pulse should be sufficiently brief in the time domain to guarantee a broad bandwidth and flat frequency response. Ideally, such a point source should be described by a delta function, $\delta(x,y,z,t)$, the practical implementation of which remains quite difficult, especially in the ultrahigh-frequency regime.

The emergence of the photoacoustic (PA) technique suggests a promising solution to overcome this challenge. As we know, the PA effect describes the phenomenon that a pulsed acoustic wave, called a PA wave, can be generated by thermoelastic expansion as the temperature rises after the absorption of a pulsed laser [22,23]. It has been widely used in biological imaging [24,25] and photoacoustic spectroscopy [26]. Focusing a laser beam through an objective lens to a diffraction-limited spot for excitation of photoacoustic waves is used in optical-resolution photoacoustic microscopy [27]. The same idea has recently been used to encode spatial information with typical time-varying photoacoustic waves for snapshot photoacoustic topography [28,29]. Due to the broad bandwidth, photoacoustics is also used for frequency calibration of ultrasonic sensors [30–32] and, obviously, the PA wave generated from a small laser spot possesses very similar behavior to that of an ideal pulsed spherical pressure wave $\delta(x,y,z,t)$.

Following this idea, we propose a method, called the PA method, that utilizes the PA waves to probe the transducer’s SIR. Here, we focus a nanosecond laser beam on an absorber to generate waterborne pulsed PA waves that mimic an ideal impulsive point acoustic source. To avoid the photobleaching effect [33] under plentiful repeated laser pulses, we choose carbon fiber with good thermal fatigue as the absorber. The SIR is directly measured by this method, by taking advantage of the 1.7 μm high spatial resolution determined by the laser spot size and the hundreds of megahertz bandwidth of the PA waves. Through two examples, we show that a transducer’s SIR can be accurately obtained by scanning the three-dimensional (3D) PA field with the transducer itself [10,34]. To reduce time consumption, the angular spectrum approach (ASA) [35,36] is also employed, which can reconstruct the entire 3D acoustic field from the measured SIR of one single near-field plane.

II. PHOTOACOUSTIC METHOD

It is a well-known fact that a linear electrical system is fully characterized by its impulse response. Applying an input signal $x(t)$ to the input of the circuit, the output $y(t)$

is then given by $y(t) = h(t)*x(t)$, where $h(t)$ is the impulse response of the linear system and “*” denotes time convolution in this paper. A linear acoustic system, for instance, a transducer radiating or receiving acoustic waves, has the same notion. Under an ideal impulse excitation $\delta(t)$, the transducer generates a pressure field that corresponds to the SIR $h(x,y,z,t)$ of the transducer. Therefore, the pressure field $p(x,y,z,t)$ radiated by the transducer is equal to the convolution of the SIR $h(x,y,z,t)$ and the driving voltage $x(t)$ [34], as given by $p(x,y,z,t) = h(x,y,z,t)*x(t)$. If the transducer works as a receiver, the same SIR $h(x,y,z,t)$ will be obtained by measuring the transducer’s response to a pulsed spherical wave $\delta(x,y,z,t)$, as a result of the reciprocity theorem [17–19]. Similarly, the output voltage $x(t)$ of the transducer is equal to the convolution of the SIR $h(x,y,z,t)$ and the pressure waves $p(x,y,z,t)$ radiated from a point acoustic source at $\mathbf{r}(x,y,z)$ relative to the transducer, namely, $x(t) = h(x,y,z,t)*p(x,y,z,t)$. We can also get the frequency response $H(x,y,z,f)$ of the transducer by decomposing the time-varying $h(x,y,z,t)$ into its constituent frequencies through Fourier transform. This means that the SIR can completely describe the radiation or receiving pattern of a transducer.

Although this notion proposed by Tupholme [20] and Stepanishen [37] has been widely used to calculate the pressure field of transducers for decades, regarding the ultrahigh-frequency range (megahertz), it is still a challenge to measure the SIR $h(x,y,z,t)$ because the realization of a pointlike detector or source becomes formidable. In this scenario, the detector or source should be small enough, together with a short response time, to approximate a delta function $\delta(x,y,z,t)$.

The PA effect provides a feasible path towards the practical realization of such impulsive point sources. It describes the process in which an absorber converts light energy into heat after light absorption, causing thermal expansion, and consequently resulting in PA waves $p_{\text{PA}} = \Gamma\eta F$ [38]. Here, Γ is a dimensionless constant called the Grüneisen parameter, F (J/m^3) is the energy-deposition density of a single laser pulse F (J/m^3) (proportional to the single-laser-pulse intensity), and η is the absorber’s conversion coefficient from light energy to wave pressure [25,39]. Due to the extremely short rise time (about 60 fs) of the waterborne PA waves exerted by a delta laser pulse [40], the bandwidth of the PA waves can reach hundreds of megahertz [34], which is far larger than those of most transducers. Unfortunately, there are no experimental reports on the measurement of the photoacoustic waveform generated from a small-volume laser spot with lengths of several microns by a nanosecond laser. Based on Ref. [40], we simplify our model and provide a primitive theoretical analysis of the photoacoustic method in Appendix B. Given the SIRs of existing commercial transducers, the PA waves can be approximately treated as pulsed spherical waves, i.e., $p_{\text{PA}}(x,y,z,t) \approx \delta(x,y,z,t)$. Inspired by the

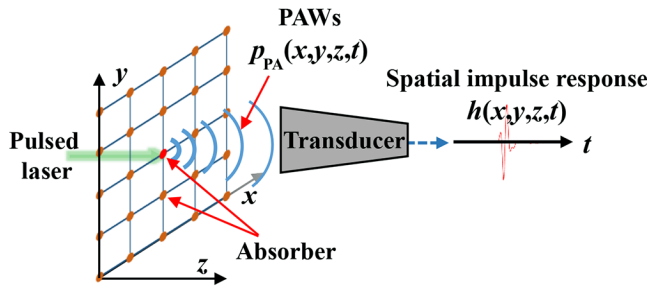


FIG. 1. Illustration of the photoacoustic method. Response of a transducer to the pulsed photoacoustic waves (PAWs) corresponds to its spatial impulse response $h(x,y,z,t)$. Focusing a pulsed laser on the absorber (here, the carbon fiber) produces the PAWs $p_{PA}(x,y,z,t)$.

abovementioned advantages, here, we focus a pulsed laser on an absorber to generate the PA waves $p_{PA}(x,y,z,t)$, as shown in Fig. 1. The SIR $h(x,y,z,t)$ is obtained by having the transducer perform measurements at a fixed position in space.

III. EXPERIMENTAL SETUP

As shown in Fig. 2(a), the system consists of three parts: laser focusing, imaging, and ultrasonic signal receiving and processing. Regarding laser focusing, the laser (1 ns pulse width and 532 nm wavelength) is expanded twofold through the L1 and L2 lens systems. Then, the beam is divided by a beam splitter (BS, Thorlabs, CM1-BP108). The reflected laser beam, accounting for 8% of the total laser energy, is detected by the photodetector (Thorlabs, PDA10A2) to trigger the oscilloscope and eliminate the deviation caused by the fluctuation of the laser energy. The rest, 92%, of the laser energy transmits through the beam splitter and is focused on a single carbon fiber of $8.7 \mu\text{m}$ in diameter by the objective lens L5 (Newport, M-20 \times) with $\text{NA} = 0.4$. The diameter of the pupil is 6 mm, and the focal length of the corresponding tube lens is 160 mm.

To ensure that the absorber is on the focal plane, we set up an imaging system to find the focal position. After being reflected by the absorber, the laser passes through the objective lens again and is reflected by the beam splitter to the planoconvex lens L3 with a focal length of 100 mm. The focal spot is then imaged by the CMOS camera

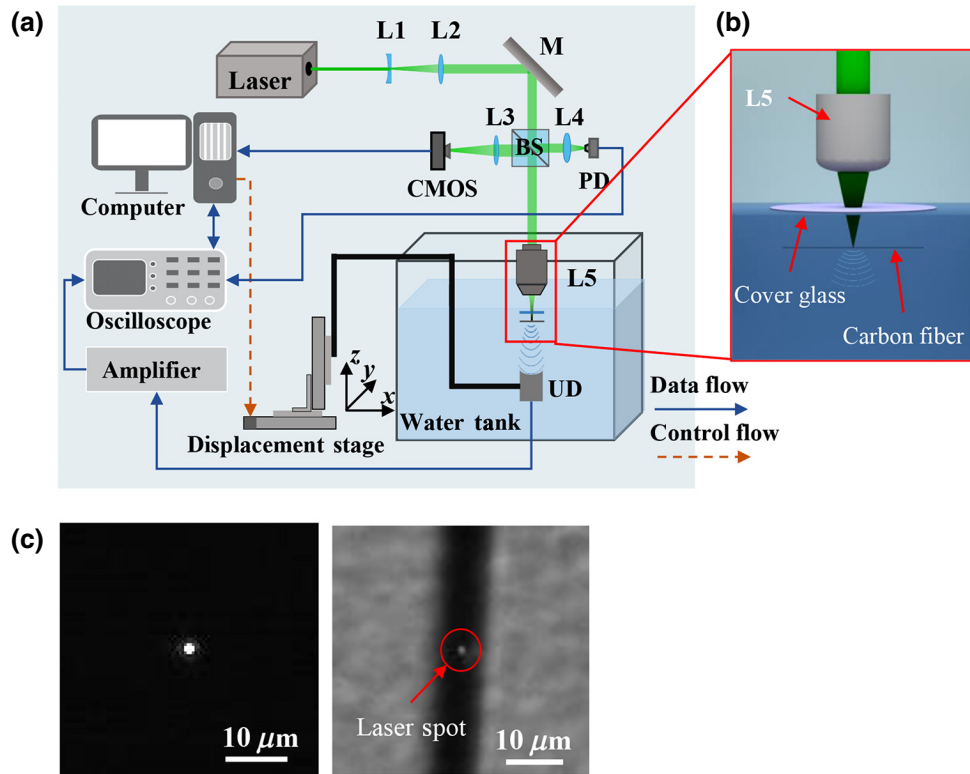


FIG. 2. Experimental setup and image of the focal spot. (a) Illustration of the experimental setup. Blue solid lines indicate the data flow, and the brown short-dashed line indicates the control flow. Laser beam is expanded by L1 and L2 and then focused by objective lens L5 on the carbon fiber to generate photoacoustic waves. Magnification of the imaging system consisting of CMOS, L3, BS, and L5 is 12.5. L1, concave lens; L2 and L4, convex lenses; L3, tube lens; L5, object lens; M, mirror; PD, photodetector; BS, beam splitter. (b) Enlarged view of the red solid region in (a). Laser beam transmits through objective lens L5 and cover glass is focused on carbon fiber immersed in degassed water. (c) Image of focal spot reflected by a mirror (left) and focal spot on carbon fiber (right). Laser spot diameter is about $1.7 \mu\text{m}$ and carbon fiber is about $8.7 \mu\text{m}$.

(Thorlabs, DCC1545m, square pixel size $5.2 \times 5.2 \mu\text{m}^2$). The magnification of the camera system is 12.5. For ultrasonic signal receiving and processing, the signal of the transducer is 50 dB and is amplified by two preamplifiers (Mini circuits, zfl-500ln+) connected in series before being sent to the digital oscilloscope (Keysight, DSO3024T). The sampling rate of the digital oscilloscope is set to 1 GSa/s, the sampling bit depth is 8 bit, and the data of each position are averaged 30 times. The data of the photodetector are also recorded by the digital oscilloscope. All devices are controlled by the computer.

The carbon fiber (Toray, T700) is used as an absorber because of its high absorption coefficient and excellent thermal fatigue [41,42]. The stability of the photoacoustic waves generated by the carbon fiber is provided in the Supplemental Material [43]. The laser beam is focused by the objective lens on the carbon fiber through a 170- μm -thick cover glass, as shown in Fig. 2(b). One side of the cover glass is exposed to air and the other side is just immersed in degassed water. The carbon fiber is also immersed in water about 1 mm beneath the cover glass. It converts the laser energy to heat immediately and causes the thermal expansion of the carbon fiber and water near the carbon fiber to generate the PA waves. The image of the laser spot reflected by a mirror is shown in the left of Fig. 2(c), and the laser spot's diameter is 1.7 μm . The image on the right of Fig. 2(c) is the laser focal spot on the carbon fiber, with a diameter of about 8.7 μm . In the experiment, the laser repetition frequency is set as 60 Hz; the output energy focused on the carbon fiber is about 20 nJ per pulse.

The BR method is employed as a benchmark to verify the practicability and effectiveness of the proposed PA method. In the BR experiment, we use a stainless-steel ball with a diameter of 2 mm as a reflector. The ultrasonic pulse-receiver Olympus 5037PR system operates under the parameters: repetition frequency, 300 Hz; energy, 1; damping, 2 (50 Ω); and gain, 39 dB. The signal acquisition and processing are the same as those of the PA method. All experiments are carried out in a tank filled with degassed water with a constant speed of sound, c (1496 m/s), and density ρ (997 kg/m³) at 25 °C.

IV. RESULTS AND DISCUSSION

Here, we measure the SIRs of two focused transducers with center frequencies 20 MHz and 93.68 MHz. We take the center point of the two transducers as the origin of the coordinates. The z -axis is perpendicular to the transducer surface, and the x - y plane is parallel to the transducer surface.

A. Acoustic field of the 20 MHz ultrasonic focused transducer

We start with a commercial cylindrical focused ultrasonic transducer, Olympus V316. According to the

specifications of the transducer, the center frequency is 20.31 MHz, the diameter of the element size is 3.175 mm, and the length of the spherical point target focus is 25.88 mm.

The measured SIR is a time-varying acoustic pressure signal. Its instantaneous amplitude has no specific physical meaning, but we can integrate the squared spatial impulse response in the time domain to obtain the acoustic intensity. For a pulsed acoustic field, here, we consider that its pressure $p(x,y,z,t)$ equals the SIR $h(x,y,z,t)$ and the acoustic intensity distribution is then given by

$$I(x,y,z) = \frac{1}{2\rho cT} \int_0^T h^2(x,y,z,t) dt, \quad (1)$$

where T is the length of the sampling time, which covers the whole time-varying SIR. The normalized acoustic intensity distributions on the x - z plane measured by the PA method and the BR method provide the lateral and axial resolution of the transducer, as shown in Fig. 3(a). The B scan, ranging from -2.5 to 2.5 mm along the x axis and 15 to 45 mm along the z axis, covers the focal spot of the transducer. The full width at half maximum (FWHM) of the acoustic intensity is about 0.6 mm in the lateral direction and about 20 mm in the axial direction, and the focal length of the transducer can be well measured at 25 mm by the two methods. The normalized acoustic intensity along the z axis, ranging from -5 to 40 mm, as shown in Fig. 3(b), displays the same results.

As mentioned above, the BR method requires the transducer to emit a pulsed wave and subsequently receive the wave reflected by a small ball. When the radius of the small ball approaches zero, the results of the BR method are close to the pulse-echo response represented by $h_{\text{PE}}(x,y,z,t)$, which is the self-convolution of the SIR $h(x,y,z,t)$ [44,45] given by

$$h_{\text{PE}}(x,y,z,t) = h(x,y,z,t) * h(x,y,z,t). \quad (2)$$

Mathematically, the normalized curve $I_{\text{PE}}(0,0,z)$ [obtained by substituting $h_{\text{PE}}(0,0,z,t)$ into Eq. (1)] is narrower than the normalized curve $I_{\text{SIR}}(0,0,z)$ [obtained by substituting $h(0,0,z,t)$ into Eq. (1)]. However, the averaging effect caused by the finite reflection area of the small ball makes the curve of $I_{\text{BR}}(0,0,z)$ broader than the curve of $I_{\text{PE}}(0,0,z)$. So, we can see that there is an overlap between the $I_{\text{PA}}(0,0,z)$ curve and the $I_{\text{BR}}(0,0,z)$ curve in the region $15 \text{ mm} < z < 32.5 \text{ mm}$.

Besides, we discuss the results from the perspective of the spectrum. It is known that a focused transducer can be simplified to a spherical curved model of opening diameter D and radius of curvature R . The monochromatic acoustic pressure as a function of distance z [46] is given by

$$p(0,0,z) = \left| k \frac{R}{R-z} \sin \frac{\pi L(R-z)}{2zR} \right|. \quad (3)$$

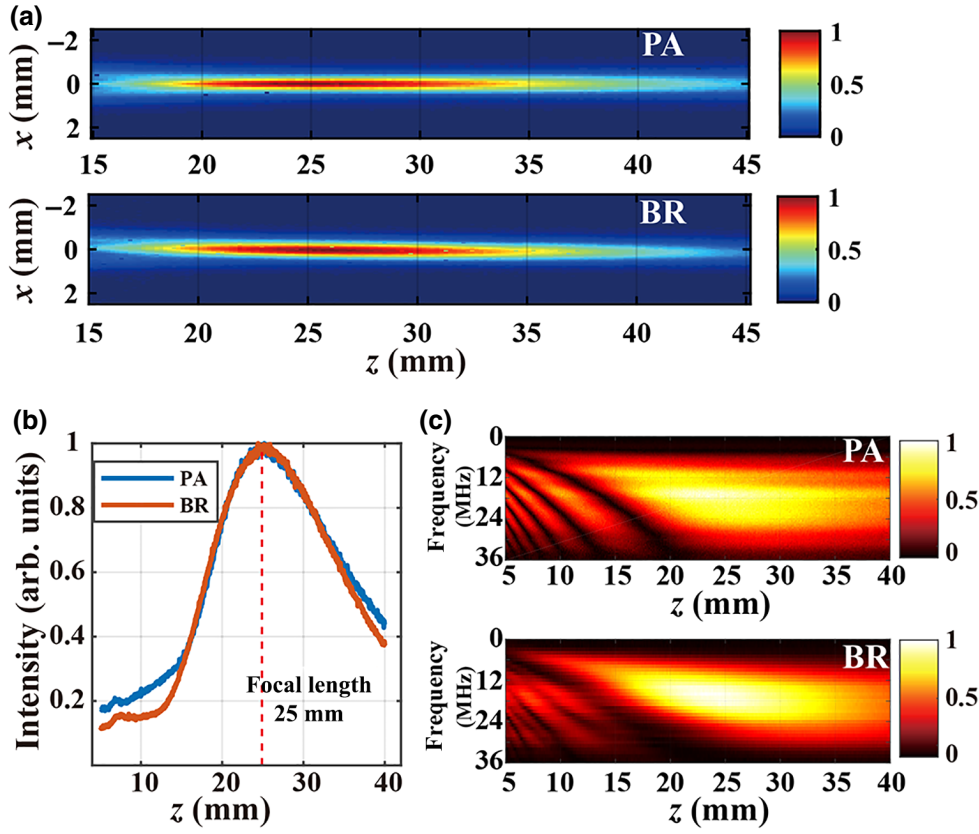


FIG. 3. Acoustic field measurements of 20 MHz focused ultrasonic transducer. (a) Normalized acoustic intensity measured by the PA method (upper) and the BR method (lower) on the x - z plane at $y = 0$. Color bar represents normalized acoustic intensity. (b) Normalized acoustic intensity along the z axis measured by the PA method (blue curve) and the BR method (brown curve). Focal length of the transducer is about 25 mm. (c) Spectrum of the SIR along the z axis. Color bar represents the normalized magnitude of the spectrum.

At the focal spot, i.e., distance z equal to the radius of curvature R , Eq. (3) reduces to $p_R = (\rho c \pi^2 L^2 / 2R^2)^{1/2}$, where $L = D^2 f / 4c$ is the transition distance of equivalent flat transducer and k is a constant. According to Eq. (3), the acoustic pressure goes through a series of maxima and minima within the distance L and one global maximum at the focus. As the frequency f increases, the oscillation of acoustic pressure versus distance z becomes fast, and the location of the last maximum increases. Although a pulsed field, like the SIR, is different from a monochromatic acoustic field, we can find characteristics similar to the monochromatic acoustic field in the frequency domain. Figure 3(c) is the spectrum of the SIR measured by the PA method (denoted by PA) and the BR method (denoted by BR) along the z axis. In the region $z > 25$ mm, the spectra of the impulse responses along the z axis obtained by the PA method and the BR method are consistent. However, in the region $z < 15$ mm, the spectrum measured by the PA method has obvious peaks and valleys. This is mainly because the PA method has a higher spatial resolution. In general, the bandwidth measured by the BR method is narrower than that measured by the PA method due to the pulse-echo process, as described in Eq. (1).

To avoid the time-consuming process on the 3D raster scanning, we use the ASA to reconstruct the 3D acoustic field based on the acoustic pressure distribution of a single plane in the near-field ($z = 3$ mm). During the near-field measurement, the grid spacing between adjacent

points is $20 \mu\text{m}$, and the measurement range in the x and y directions is -2.5 to 2.5 mm. The ASA-reconstructed results are compared with those directly measured using the PA method. Figure 4(a) shows the acoustic intensity distributions at $z = 5, 15,$ and 25 mm measured by the PA method with a grid spacing of 0.1 mm. Figure 4(b) shows the acoustic intensity distributions at $z = 5, 15,$ and 25 mm reconstructed by the ASA method. A comparison of the acoustic intensity profiles obtained with both methods along the x axis at $y = 0$ is further presented in Fig. 4(c). It is found that the two results are in good agreement, proving the accuracy and efficiency of both the PA method and the ASA-based acoustic field reconstruction. Comparing the reconstructed acoustic intensity based on data measured by the PA method and the BR method, we further confirm the applicability of the PA method, and a detailed description is given in the Supplemental Material [43].

B. Acoustic field of the 93 MHz ultrasonic focused transducer

Ultrahigh-frequency ultrasonic field measurements have rarely been reported. Here, we use the PA method to measure the acoustic field of the Olympus V3346 transducer. According to the specifications of the transducer, the center frequency is 93.68 MHz, the diameter of the element

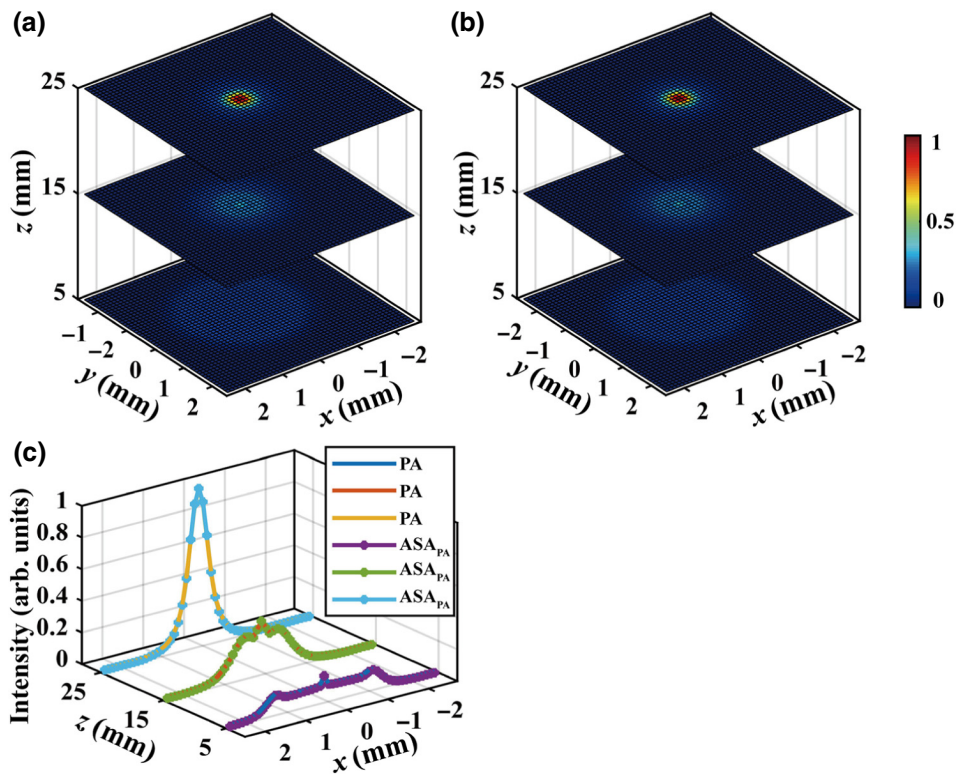


FIG. 4. Acoustic intensity distributions of 20 MHz focused ultrasonic transducer on the x - y plane at $z = 5, 15,$ and 25 mm. Results (a) measured by the PA method and (b) reconstructed by the ASA. Color bar represents normalized acoustic intensity. (c) Acoustic intensity profile along the x axis at $y = 0$. ASA results are calculated based on measured SIR (using the PA method) on the x - y plane at $z = 3$ mm.

size is 3.175 mm, and the length of the spherical optical limit focus is about 6.73 mm.

The acoustic intensity along the z axis (cyan curve) is provided in Fig. 5(a), in which the measured focal length is 6.5 mm, which is consistent with the factory parameters of the transducer. The spectrum (hot colormap) of the SIR along the z axis is also shown in Fig. 5(a). Because of the filtering effect of the transducer’s transmitting aperture, the 62 MHz maximum center frequency of the SIR at $z = 6.5$ mm is less than that of 93.68 MHz measured by the BR method using a large ball as an equal-phase reflector near the transmitting surface. We analyze the monochromatic normalized acoustic pressure along the z axis at frequencies $f = 40, 60, 80,$ and 100 MHz, as shown in

Fig. 5(b). Due to the poor resolution of an 8 bit digital-to-analog conversion of the oscilloscope and the noise influence, it is hard to distinguish the oscillation of the acoustic pressure far away from the focus. Nevertheless, we can see that the acoustic pressure oscillates near the focus and reaches the maximum at the focus. As the frequency increases, the axial width of focus gets narrower and the oscillation period of the acoustic pressure versus distance z becomes shorter. These characteristics are consistent with theory.

Figure 6(a) shows the acoustic intensity distributions on the x - y plane at $z = 6.2, 6.5,$ and 6.8 mm. The grid spacing is $10 \mu\text{m}$, and the measurement range is -0.25 to 0.25 mm in both x and y directions. Figure 6(b) is the

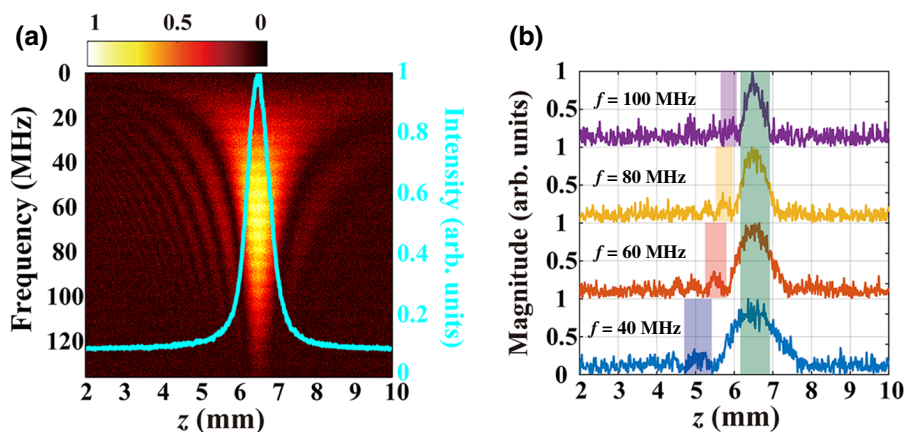


FIG. 5. Acoustic field of 93 MHz focused ultrasonic transducer along z axis measured by the PA method. (a) Normalized acoustic intensity versus z -axis curve (cyan solid) and spectrum (hot colormap) of SIR along the z axis. Color bar represents normalized magnitude of the spectrum. (b) Monochromatic normalized acoustic pressure along the z axis at frequencies $f = 40, 60, 80,$ and 100 MHz.

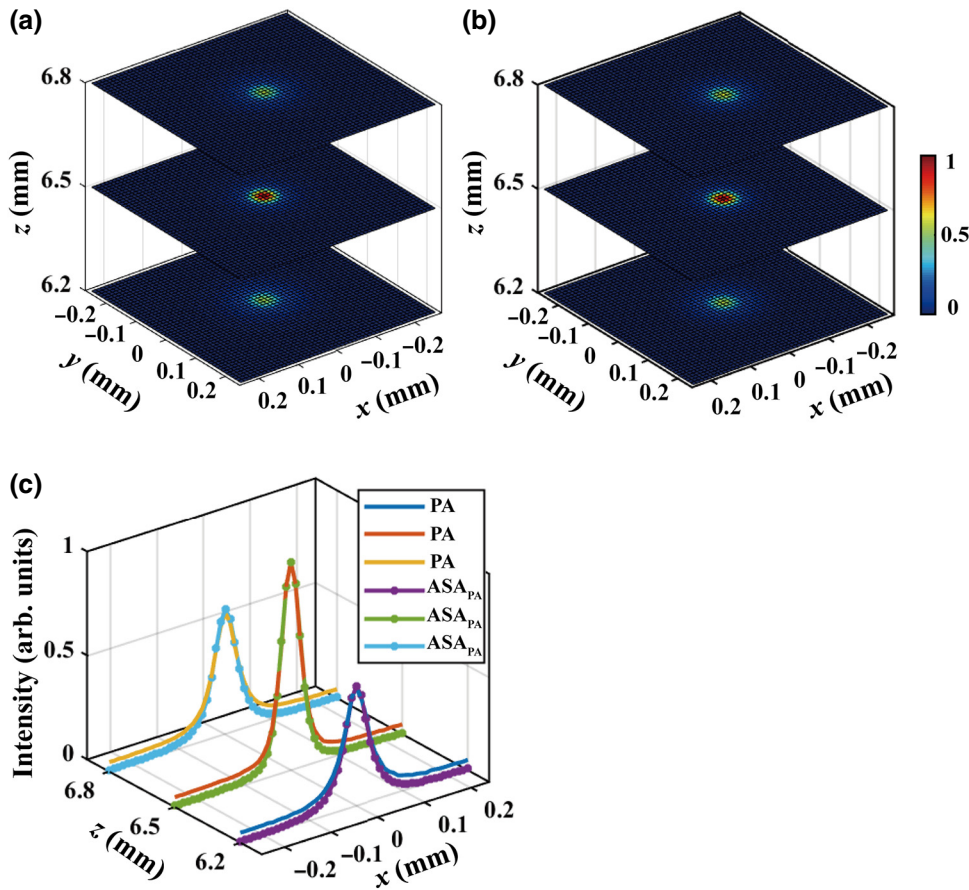


FIG. 6. Acoustic intensity distributions of 93 MHz focused ultrasonic transducer on x - y plane at $z = 6.2, 6.5,$ and 6.8 mm. Results (a) measured by the PA method and (b) calculated by the ASA. Color bar represents normalized acoustic intensity. (c) Acoustic intensity profile along the x axis at $y = 0$. ASA results are calculated based on measured SIR (using the PA method) on x - y plane at $z = 2$ mm.

acoustic intensity reconstructed by the ASA based on the x - y plane SIR at $z = 2$ mm. The grid spacing between adjacent points is $10 \mu\text{m}$, and the measurement range in the x and y directions is -2 to 2 mm. The two groups of intensity profiles along the x axis at $y = 0$ are consistent with each other, as shown in Fig. 6(c).

V. CONCLUSIONS

The PA effect enables the practical realization of a point acoustic source emitting extremely short-duration pulses that are essential for the characterization of ultrahigh-frequency ultrasonic transducers. We measure the SIRs of two commercial ultrasonic transducers (20 and 93 MHz) based on the proposed PA method. The results confirm the advantages of this strategy over conventional methods for the following aspects: (i) The spatial resolution of sampling the acoustic field is determined by the laser spot size, rather than the detection area of the hydrophone or the effective reflection area of the small ball. Here, we achieve $1.7 \mu\text{m}$ spatial resolution, which is far beyond that of $40 \mu\text{m}$ spatial resolution of the state-of-art commercial hydrophone. (ii) By operating in receive mode, the PA method provides a way to characterize some receive-only ultrasonic detectors, for instance, acoustic detection technologies based on Fabry-Perot interferometers and

microring resonators. (iii) Without an actual probe required by the HP and BR methods, the PA method avoids the disturbance of the acoustic field induced by unwanted scattering. Therefore, we believe the superior performance of the proposed PA method will bring exciting opportunities to a wide variety of fields, such as transducer design, nondestructive evaluation, and biomedical ultrasound.

ACKNOWLEDGMENTS

This work is supported by the National Key R&D Program of China (Grants No. 2017YFA0303702 and No. 2018YFA0306200), the National Natural Science Foundation of China (Grants No. 11625418, No. 11774297, No. 51732006, No. 11890700, and No. 51721001), and the Scientific Research Foundation of Graduate School of Nanjing University.

APPENDIX A: RERADIATION METHOD BASED ON ANGULAR SPECTRUM APPROACH

Raster scanning the 3D acoustic field generated by a transducer is a highly time-consuming process. For homogeneous media, several projection methods are proposed to reconstruct the 3D acoustic field based on single-plane measurements, such as the ASA [36] and Rayleigh integrals [47] in the linear regime. These methods greatly

improve the speed of obtaining the 3D acoustic field of transducers, but require high spatial resolution during the single-plane measurement.

Here, we choose the ASA because it has a faster calculation speed. Given that the measured SIR data on the $z = z_0$ plane is discrete, to ensure the accuracy of the reconstructed field, the grid spacing within the x - y plane should be less than 0.8λ [48]. For example, the grid spacing of 20 and 100 MHz center frequency transducers are less than 60 and 12 μm , respectively, which is below the resolution limit of the traditional hydrophone or small-ball reflection methods. The proposed photoacoustic source with a diameter of 1.7 μm can go beyond this limit and acts as a nearly ideal point source.

In Fourier acoustics, the ASA is often used to calculate the sound radiation and near-field acoustical holography [49]. First, the near-field SIR $p(x, y, z_0, t)$ on the x - y plane of $z = z_0$ is measured. It is then mirrored in time, i.e., $p(x, y, z_0, -t)$, and transformed to the frequency domain as

$$P(x, y, z_0, \omega) = F_t[p(x, y, z_0, -t)]. \quad (\text{A1})$$

The angular spectrum of the acoustic field on an arbitrary plane can be determined from the angular spectrum on the measurement plane:

$$P(k_x, k_y, z_0, \omega) = F_x F_y [P(x, y, z_0, \omega)]. \quad (\text{A2})$$

The wave propagation from $z = z_0$ to $z = z_1$ results in not only the phase shift, but also in ultrasonic attenuation in water. The phase shift is $\exp[ik_z(z_1 - z_0)]$, and the attenuation factor in the ASA is related to the wave vector. For the wave vector k_z , the attenuation term is equal to $\exp[-\alpha(k/k_z)(z_1 - z_0)]$, where $k = \omega/c$ and $k^2 = k_x^2 + k_y^2 + k_z^2$. α is the attenuation coefficient (dB/m) in 25 $^\circ\text{C}$ degassed water. It is frequency dependent and can be calculated by seventh order polynomial fitting [50]. The angular spectrum at $z = z_1$ is as follows:

$$P(k_x, k_y, z_1, \omega) = P(k_x, k_y, z_0, \omega) \exp[ik_z(z_1 - z_0)] \exp\left[-\frac{\alpha(z_1 - z_0)k}{k_z}\right]. \quad (\text{A3})$$

Finally, the angular spectrum at $z = z_1$ can be inversely transformed into the time-space domain as

$$p(x, y, z_1, t) = F_t^{-1} F_x^{-1} F_y^{-1} [P(k_x, k_y, z_1, \omega)]. \quad (\text{A4})$$

APPENDIX B: A THEORETICAL ANALYSIS OF THE PHOTOACOUSTIC METHOD

As we know, the impulse response of the transducer to a delta pulsed spherical wave yields the corresponding spatial impulse response, and the SIR can be calculated by

integration on the surface of the transducer, as given by

$$h(\vec{r}, t) = E_m(t) * \iint_S \frac{1}{2\pi |\vec{r} - \vec{r}_1|} \delta\left(t - \frac{|\vec{r} - \vec{r}_1|}{c}\right) dS \quad (\text{B1})$$

where $E_m(t)$ and S indicate the electromechanical impulse response and detection surface of the transducer, respectively; \vec{r} indicates the source of the ideal pulsed spherical wave; \vec{r}_1 indicates one point of the transducer surface; and c is the speed of sound. In the photoacoustic method, we use the photoacoustic waves as a substitute for the pulsed spherical waves, $\delta(x, y, z, t)$. The relationship between the measured SIR using the photoacoustic method and the actual SIR is discussed in the following.

We consider the photoacoustic waves generated from a point source by long Gaussian optical pulses taking the form $I(t) \propto \exp\left[-\left(\frac{t}{\theta}\right)^2\right]$. As reported in Ref. [40], the photoacoustic waves can be divided into two mechanisms: the linear sound-generation mechanism gives bipolar photoacoustic waves and the nonlinear mechanism produces asymmetric tripolar waves. When the transducer detects the photoacoustic waves generated from a small volume V , the output signal $O(\vec{r}, t)$ of the transducer is the superposition of the photoacoustic waves generated by all photoacoustic point sources and can be calculated by the Rayleigh integral:

$$O(\vec{r}, t) = E_m * \iint_S dS \times \iiint_V \frac{p_L\left(t - \frac{|\vec{r} - \vec{r}_1 + \delta\vec{r}_2|}{c}\right) + p_N\left(t - \frac{|\vec{r} - \vec{r}_1 + \delta\vec{r}_2|}{c}\right)}{2\pi |\vec{r} - \vec{r}_1 + \delta\vec{r}_2|} dV, \quad (\text{B2})$$

where \vec{r} indicates the reference point in the photoacoustic source, \vec{r}_1 indicates the point on the transducer surface, and $\delta\vec{r}_2$ indicates a photoacoustic point source relative to the reference point. The linear photoacoustic waves, p_L , and nonlinear photoacoustic waves, p_N , are given by [40]

$$p_L(\tau) = \frac{-\tau E(\vec{r}) \beta_1}{c_p \theta^3} \exp\left[-\left(\frac{\tau}{\theta}\right)^2\right], \quad (\text{B3})$$

$$p_N(\tau) = \frac{E(\vec{r})^2 \beta_2}{64\pi^2 c_p^2 \alpha^{1.5} \rho \theta^{1.5}} \frac{\partial^2 \left\{ \exp\left[-2\left(\frac{\tau}{\theta}\right)^2\right] \right\}}{\partial \tau^2} \times \int_0^\infty \left[\frac{\text{erf}\left(\frac{\xi}{\sqrt{2}}\right)}{\xi^{1.5}} \right] \exp\left(2\xi \frac{\tau}{\theta} - \frac{\xi^2}{2}\right) d\xi, \quad (\text{B4})$$

where E , c_p , α , ρ , and θ are the heat energy of a single pulse, the isobaric heat capacity, the thermal diffusivity, the density, and the laser pulse time duration, respectively. β_1 and β_2 are the first two coefficients in a power series expansion of the thermal expansion coefficient, and τ is given by $\tau = (t - |\vec{r} - \vec{r}_1 + \delta\vec{r}_2|/c)$. The output signal is then evaluated by introducing a time convolution with a delta function in Eq. (B2) and substituting Eq. (B1), as given by

$$O(\vec{r}, t) = E_m * \iint_S dS \iiint_V dV \times \int_{-\infty}^{\infty} \frac{\delta\left(t - t' - \frac{|\vec{r} - \vec{r}_1|}{c}\right)}{2\pi |\vec{r} - \vec{r}_1|} \frac{|\vec{r} - \vec{r}_1|}{|\vec{r} - \vec{r}_1 + \delta\vec{r}_2|} [p_L(\tau') + p_N(\tau')] dt', \quad (\text{B5})$$

where $\tau' = t' - [(|\vec{r} - \vec{r}_1 + \delta\vec{r}_2| - |\vec{r} - \vec{r}_1|)/c]$. Because the volume of the photoacoustic source is much smaller than the wavelength, for any point in the photoacoustic source $|\vec{r} - \vec{r}_1| \gg |\delta\vec{r}_2|$, we can consider that $(|\vec{r} - \vec{r}_1 + \delta\vec{r}_2|)/(|\vec{r} - \vec{r}_1|) \approx 1$ and $\tau' \approx t' - [|\delta\vec{r}_2|\cos\theta]/c$, where θ is the angle between vector $\vec{r} - \vec{r}_1$ and vector $\delta\vec{r}_2$. Here, θ is independent of \vec{r}_1 , as long as the aperture of the transducer is small enough compared with the distance from the transducer to the photoacoustic

source. Therefore, Eq. (B5) can be written as

$$O(\vec{r}, t) \approx h(\vec{r}, t) * \iiint_V \left[p_L\left(t - \frac{|\delta\vec{r}_2|\cos\theta}{c}\right) + p_N\left(t - \frac{|\delta\vec{r}_2|\cos\theta}{c}\right) \right] dV. \quad (\text{B6})$$

The spectrum can be obtained through Fourier transform on the two sides of Eq. (B6). The spectrum of the photoacoustic wave, which depends on the angle θ , is given by

$$H(\theta, f) = F_t \left\{ \iiint_V \left[p_L\left(t - \frac{|\delta\vec{r}_2|\cos\theta}{c}\right) + p_N\left(t - \frac{|\delta\vec{r}_2|\cos\theta}{c}\right) \right] dV \right\}, \quad (\text{B7})$$

where f indicates frequency. If the spectrum function $H(\theta, f)$ has a broad bandwidth and relatively flat frequency response, the output signal approximately equals the actual spatial impulse response, as given by $h(\vec{r}, t) \approx O(\vec{r}, t)$.

Before calculating it, we should find out the spatial distribution of the photoacoustic source. Once focusing the laser beam with an objective lens on the carbon fiber, most of the light energy (about 85%) is absorbed by

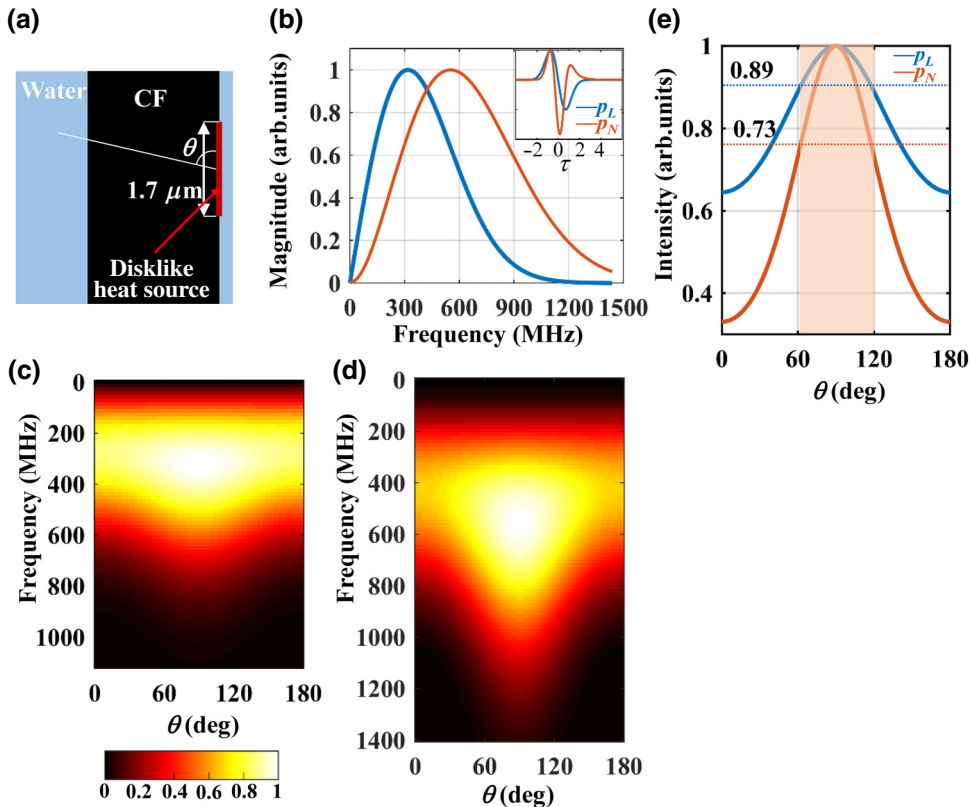


FIG. 7. (a) Cross section of the thin disklike heat source. CF, carbon fiber. (b) Normalized spectrum of the bipolar waves (blue curve) and tripolar waves (brown curve) generated from a point source; the waveform is shown in the inset. Normalized spectrum of the photoacoustic waves generated by the thin disklike heat source contributed to by the bipolar waves (c) and tripolar waves (d) versus the angle θ . Color bar represents the normalized magnitude of the spectrum. (e) Directivity of the two-dimensional disk photoacoustic source. Angle θ is shown in (a).

the carbon fiber, and its strong absorption prevents the light from penetrating to the deep regions of the carbon fiber. So, the spatial distribution of absorbed light has the same cross-section area as that of the laser spot, but a much smaller depth and almost simultaneously most energy of the absorbed light is converted into heat [51]. Subsequently, the heat diffuses within the carbon fiber and outwardly into the surrounding water. For a 1-ns-pulse-width laser, the thermal diffusion length L during the pulse period can be estimated from $L = 2\sqrt{\alpha\delta_t}$, where α and δ_t are the thermal diffusivity and pulse duration of the laser (10^{-9} s). Thus, the thermal diffusion lengths in water (the thermal diffusivity is $0.146 \text{ mm}^2/\text{s}$, 25°C) and carbon fiber (the thermal diffusivity parallel to the fiber plane is $1.77 \text{ mm}^2/\text{s}$, 25°C) are 24 and 84 nm, respectively, which are negligible relative to the laser spot size. So, we can treat the area of the laser spot on the carbon fiber as a very thin disklike heat source or photoacoustic source. The photoacoustic source and its cross section are shown in Fig. 7(a). The cross section is the cutting plane perpendicular to the laser spot and passing through the center of the laser spot.

With the release of heat, the increase in temperature causes thermal expansion of carbon fiber and water. In Eqs. (B3) and (B4), we find that the photoacoustic pressure depends on the physical properties of the medium and the photoacoustic waveform is only related to the long Gaussian optical pulses. The above conclusions are discussed in Ref. [52], and these treatments avoid the complicated analysis of heat transfer from the carbon fiber to water. Thus, the photoacoustic waves at a space point are the superposition of those generated from carbon fiber and water with different weights.

First, we calculate the waterborne photoacoustic waves generated from a point source with Eqs. (B3) and (B4). We take the laser pulse width $\theta = 1 \times 10^{-9}/\sqrt{2}$ s, $E = 3$ fJ, and β_1 and β_2 can be calculated by the linear fitting. The waveform and its spectrum are shown in the inset of Figs. 7(b) and in Fig. 7(b). The center frequencies of the linear part (blue curve) and the nonlinear part (brown curve) are 317.2 and 552.0 MHz, respectively. The bandwidths of -6 dB are 102 to 610 MHz and 247 to 955 MHz, which are broad enough to cover the spatial impulse response of the high-frequency transducer.

In the photoacoustic method, the photoacoustic waveform and its spectrum vary with the angle θ , as shown in Eq. (B7). Here, we simplify the three-dimensional heat source to a two-dimensional uniform disk heat source, with $1.7 \mu\text{m}$ diameter, by neglecting the thickness of the heat source. The spectra of the bipolar waves and tripolar waves versus angle θ are shown in Figs. 7(c) and 7(d), respectively. When the angle $\theta = 90^\circ$, the bandwidth of -6 dB reaches a maximum, which is consistent with the photoacoustic point sources for bipolar waves and tripolar waves shown in Fig. 7(b). As the angle is away from 90° , the spectrum varies symmetrically, and the bandwidth

gradually gets narrower. The transducer is generally located within the angle of 60° to 120° . The bandwidths of -6 dB at 60° or 120° range from 99.0 to 586 MHz and from 226.3 to 876.8 MHz for bipolar waves and tripolar waves, respectively. Although the bandwidths of both waves slightly narrow down, and the center frequencies shift to low frequency, with the variation of angle θ , their bandwidths are still broad enough for high-frequency transducers. Additionally, the intensity of the photoacoustic waves also depends on the angle θ , as seen from the directivity shown in Fig. 7(e). The intensity is maintained above 0.89 relative to the maximum intensity for bipolar waves and 0.73 for tripolar waves at the angle range from 60° to 90° .

In general, when the temperature rise is slight, the linear bipolar waves dominate the photoacoustic waves and vice versa. Both bipolar waves and tripolar waves generated from a small volume have sufficient bandwidth to probe the spatial impulse response of the high-frequency transducer. For lower-frequency transducers, we should change the pulse duration of the laser or the size of the laser spot to shift the spectrum of the photoacoustic waves to suit the bandwidth range of low-frequency transducers.

-
- [1] L. V. Wang and S. Hu, Photoacoustic tomography: In vivo imaging from organelles to organs, *science* **335**, 1458 (2012).
 - [2] B. W. Drinkwater and P. D. Wilcox, Ultrasonic arrays for non-destructive evaluation: A review, *Ndt & E International* **39**, 525 (2006).
 - [3] K. K. Shung, *Diagnostic Ultrasound: Imaging and Blood Flow Measurements* (CRC press, 2015).
 - [4] P. Brassier, B. Hosten, and F. Vulovic, High-frequency transducers and correlation method to enhance ultrasonic gas flow metering, *Flow Meas. Instrum.* **12**, 201 (2001).
 - [5] K. Nakamura, *Ultrasonic Transducers: Materials and Design for Sensors, Actuators and Medical Applications* (Elsevier, 2012).
 - [6] K. K. Shung, J. Cannata, and Q. Zhou, Piezoelectric materials for high frequency medical imaging applications: A review, *J. Electroceram.* **19**, 141 (2007).
 - [7] C. Zhang, T. Ling, S.-L. Chen, and L. J. Guo, Ultrabroad bandwidth and highly sensitive optical ultrasonic detector for photoacoustic imaging, *ACS Photonics* **1**, 1093 (2014).
 - [8] J. F. Synnevag, A. Austeng, and S. Holm, Adaptive beamforming applied to medical ultrasound imaging, *IEEE Trans. Ultrason., Ferroelectr., Freq. Control* **54**, 1606 (2007).
 - [9] M. O'Donnell and Y. Wang, Coded excitation for synthetic aperture ultrasound imaging, *IEEE Trans. Ultrason., Ferroelectr., Freq. Control* **52**, 171 (2005).
 - [10] J. A. Jensen and N. B. Svendsen, Calculation of pressure fields from arbitrarily shaped, apodized, and excited ultrasound transducers, *IEEE Trans. Ultrason., Ferroelectr., Freq. Control* **39**, 262 (1992).
 - [11] B. E. Treeby, J. Budisky, E. S. Wise, J. Jaros, and B. Cox, Rapid calculation of acoustic fields from arbitrary

- continuous-wave sources, *J. Acoust. Soc. Am.* **143**, 529 (2018).
- [12] B. Huang and K. K. Shung, Characterization of high-frequency, single-element focused transducers with wire target and hydrophone, *IEEE Trans. Ultrason., Ferroelectr., Freq. Control* **52**, 1608 (2005).
- [13] K. Raum and W. D. O'Brien, Pulse-echo field distribution measurement technique for high-frequency ultrasound sources, *IEEE Trans. Ultrason., Ferroelectr., Freq. Control* **44**, 810 (1997).
- [14] E. Radulescu, P. Lewin, A. Nowicki, and W. Berger, Hydrophones' effective diameter measurements as a quasi-continuous function of frequency, *Ultrasonics* **41**, 635 (2003).
- [15] S. Umchid, R. Gopinath, K. Srinivasan, P. Lewin, A. Daryoush, L. Bansal, and M. El-Sherif, Development of calibration techniques for ultrasonic hydrophone probes in the frequency range from 1 to 100 MHz, *Ultrasonics* **49**, 306 (2009).
- [16] H. Khelladi and H. Djelouah, The size effects of a rigid reflector in the scattering of transient ultrasonic field, *Ultrasonics* **37**, 697 (2000).
- [17] L. E. Kinsler, A. R. Frey, A. B. Coppens, and J. V. Sanders, *Fundamentals of Acoustics*, *Fundamentals of Acoustics*, 4th Edition, by Lawrence E. Kinsler, Austin R. Frey, Alan B. Coppens, James V. Sanders, pp. 560. Wiley-VCH, (1999), p. 560. ISBN 0-471-84789-5, December 1999.
- [18] F. Fahy, Some applications of the reciprocity principle in experimental vibroacoustics, *Acoust. Phys.* **49**, 217 (2003).
- [19] J. Weight and A. Hayman, Observations of the propagation of very short ultrasonic pulses and their reflection by small targets, *J. Acoust. Soc. Am.* **63**, 396 (1978).
- [20] G. E. Topholme, Generation of acoustic pulses by baffled plane pistons, *Mathematika* **16**, 209 (1969).
- [21] P. R. Stepanishen, Transient radiation from pistons in an infinite planar baffle, *J. Acoust. Soc. Am.* **49**, 1629 (1971).
- [22] M. Xu and L. V. Wang, Photoacoustic imaging in biomedicine, *Rev. Sci. Instrum.* **77**, 041101 (2006).
- [23] A. Rosencwaig and A. Gersho, Theory of the photoacoustic effect with solids, *J. Appl. Phys.* **47**, 64 (1976).
- [24] L. V. Wang and J. Yao, A practical guide to photoacoustic tomography in the life sciences, *Nat. Methods* **13**, 627 (2016).
- [25] Y. Zhou, J. Yao, and L. V. Wang, Tutorial on photoacoustic tomography, *J. Biomed. Opt.* **21**, 61007 (2016).
- [26] P. Patimisco, G. Scamarcio, F. K. Tittel, and V. Spagnolo, Quartz-enhanced photoacoustic spectroscopy: A review, *Sensors* **14**, 6165 (2014).
- [27] S. Hu, K. Maslov, and L. V. Wang, Second-generation optical-resolution photoacoustic microscopy with improved sensitivity and speed, *Opt. Lett.* **36**, 1134 (2011).
- [28] Y. Li *et al.*, Snapshot photoacoustic topography through an ergodic relay for high-throughput imaging of optical absorption, *Nat. Photonics* **14**, 164 (2020).
- [29] X. L. Deán-Ben, A. Özbek, H. López-Schier, and D. Razansky, Acoustic Scattering Mediated Single Detector Photoacoustic Tomography, *Phys. Rev. Lett.* **123**, 174301 (2019).
- [30] Q. Sheng, K. Wang, T. P. Matthews, J. Xia, L. Zhu, L. V. Wang, and M. A. Anastasio, A constrained variable projection reconstruction method for photoacoustic computed tomography without accurate knowledge of transducer responses, *IEEE Trans. Med. Imaging* **34**, 2443 (2015).
- [31] L. Li *et al.*, Single-impulse panoramic photoacoustic computed tomography of small-animal whole-body dynamics at high spatiotemporal resolution, *Nat. Biomed. Eng.* **1**, 0071 (2017).
- [32] A. Rosenthal, V. Ntziachristos, and D. Razansky, Optoacoustic methods for frequency calibration of ultrasonic sensors, *IEEE Trans. Ultrason., Ferroelectr., Freq. Control* **58**, 316 (2011).
- [33] J. Yao, L. Wang, C. Li, C. Zhang, and L. V. Wang, Photoimprint Photoacoustic Microscopy for Three-Dimensional Label-Free Subdiffraction Imaging, *Phys. Rev. Lett.* **112**, 014302 (2014).
- [34] J. r and A. Jensen, A new calculation procedure for spatial impulse responses in ultrasound, *J. Acoust. Soc. Am.* **105**, 3266 (1999).
- [35] T. Marhenke, S. J. Sanabria, B. R. Chintada, R. Furrer, J. Neuenschwander, and O. Goksel, Acoustic field characterization of medical array transducers based on unfocused transmits and single-plane hydrophone measurements, *Sensors* **19**, 863 (2019).
- [36] Y. Du, H. Jensen, and J. A. Jensen, Investigation of an angular spectrum approach for pulsed ultrasound fields, *Ultrasonics* **53**, 1185 (2013).
- [37] P. R. Stepanishen, The time-dependent force and radiation impedance on a piston in a rigid infinite planar baffle, *J. Acoust. Soc. Am.* **49**, 841 (1971).
- [38] V. E. Gusev and A. A. Karabutov, in *Laser optoacoustics*, (AIP, New York, 1993), Chap. 1.
- [39] J. Xia, J. Yao, and L. V. Wang, Photoacoustic tomography: Principles and advances, *Electromag. Waves (Cambridge, Mass.)* **147**, 1 (2014).
- [40] I. G. Calasso, W. Craig, and G. J. Diebold, Photoacoustic Point Source, *Phys. Rev. Lett.* **86**, 3550 (2001).
- [41] X. Huang, Fabrication and properties of carbon fibers, *Materials* **2**, 2369 (2009).
- [42] D. Edie, The effect of processing on the structure and properties of carbon fibers, *Carbon* **36**, 345 (1998).
- [43] See the Supplemental Material at <http://link.aps.org/supplemental/10.1103/PhysRevApplied.14.034026> for supporting measurements and a comparison of the PA method and the BR method.
- [44] A. Lhémy, Impulse-response method to predict echo-responses from targets of complex geometry. part I: Theory, *J. Acoust. Soc. Am.* **90**, 2799 (1991).
- [45] M. Sandell and A. Grennberg, Estimation of the spatial impulse response of an ultrasonic transducer using a tomographic approach, *J. Acoust. Soc. Am.* **98**, 2094 (1995).
- [46] G. Kossoff, Analysis of focusing action of spherically curved transducers, *Ultrasound Med. Biol.* **5**, 359 (1979).
- [47] O. A. Sapozhnikov, S. A. Tsysar, V. A. Khokhlova, and W. Kreider, Acoustic holography as a metrological tool for characterizing medical ultrasound sources and fields, *J. Acoust. Soc. Am.* **138**, 1515 (2015).
- [48] D. Baker, Determination of Far-field characteristics of large underwater sound transducers from near-field measurements, *J. Acoust. Soc. Am.* **34**, 1737 (1962).

- [49] E. G. Williams, *Fourier Acoustics: Sound Radiation and Nearfield Acoustical Holography* (Elsevier, 1999).
- [50] J. Pinkerton, The absorption of ultrasonic waves in liquids and its relation to molecular constitution, *Proc. Phys. Soc. Sec. B* **62**, 129 (1949).
- [51] P. W. Beaumont, C. Soutis, and A. Hodzic, *The Structural Integrity of Carbon Fiber Composites: Fifty Years of Progress and Achievement of the Science, Development, and Applications* (Springer, 2016).
- [52] F. Gao, R. Kishor, X. Feng, S. Liu, R. Ding, R. Zhang, and Y. Zheng, An analytical study of photoacoustic and thermoacoustic generation efficiency towards contrast agent and film design optimization, *Photoacoustics* **7**, 1 (2017).